ACSNANO Cite This: ACS Nano 2018, 12, 7239−7245 www.acsnano.org

ARTICLE

High-Performance Near-Infrared Photodetectors Based on p-Type SnX (X = S, Se) Nanowires Grown *via* Chemical Vapor Deposition

Dingshan Zheng,[†,‡,¶] Hehai Fang,[†,§,¶] Mingsheng Long,[*,†] Feng Wu,[†] Peng Wang,[†] Fan Gong,[†] Xing Wu,[∥] Johnny C. Ho,[⊥] Lei Liao,[*,#] and Weida Hu[*,†,§]

[†]State Key Laboratory of Infrared Physics, Shanghai Institute of Technical Physics, Chinese Academy of Sciences, Shanghai 200083, China

[‡]School of Physics and Optoelectronic Engineering, Yangtze University, Jingzhou 434023, China

[§]University of Chinese Academy of Sciences, Beijing 100049, China

[#]State Key Laboratory for Chemo/Biosensing and Chemometrics, School of Physics and Electronics, Hunan University, Changsha 410082, China

[⊥]Department of Materials Science and Engineering, City University of Hong Kong, Hong Kong SAR, China

[∥]Key Laboratory of Polar Materials and Devices of MOE, East China Normal University, Shanghai 200241, China

Supporting Information

ABSTRACT: Because of the distinct electronic properties and strong interaction with light, quasi-one-dimensional nanowires (NWs) with semiconducting property have been demonstrated with tremendous potential for various technological applications, especially electronics and optoelectronics. However, until now, most of the state-of-the-art NW photodetectors are predominantly based on the n-type NW channel. Here, we successfully synthesized p-type SnSe and SnS NWs *via* the chemical vapor deposition method and fabricated high-performance single SnSe and SnS NW photodetectors. Importantly, these two NW devices exhibit an impressive photodetection performance with a high photoconductive gain of 1.5×10^4 (2.8×10^4), good responsivity of 1.0×10^4 A W^{-1} (1.6×10^4 A W^{-1}), and excellent detectivity of 3.3×10^{12} Jones (2.4×10^{12} Jones) under near-infrared illumination at a bias of 3 V for the SnSe NW (SnS NW) channel. The rise and fall times can be as efficient as 460 and 520 μs (1.2 and 15.1 ms), respectively, for the SnSe NW (SnS NW) device. Moreover, the spatially resolved photocurrent mapping of the devices further reveals the bias-dependent photocurrent generation. All these results evidently demonstrate that the p-type SnSe and SnS NWs have great potential to be applied in next-generation high-performance optoelectronic devices.

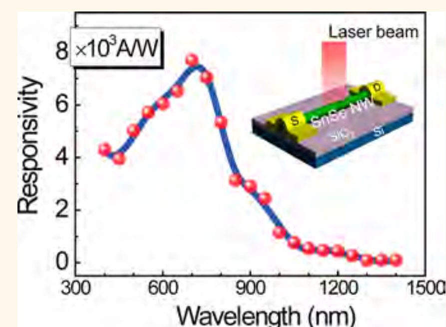

KEYWORDS: *SnSe, SnS, nanowire, chemical vapor deposition, near-infrared photodetector*

In recent years, due to the large surface-to-volume ratio, high carrier mobility, tunable light absorption, and considerable subwavelength size effect at room temperature,[1−5] quasi-one-dimensional nanowires (NWs) with semiconducting property have been widely investigated as active materials for high-performance photodetectors. When configured into devices, these NW detectors exhibit excellent optoelectronic characteristics with ultrahigh optical gain, controllable spectrum sensitivity, large photoresponse bandwidth, and considerable light-to-current conversion efficiency.[5−8] Among many nanomaterials, IV−VI semiconductor nanomaterials with narrow band gaps, such as SnS,[9−11] SnS_2,[12,13] SnSe,[14−16] $SnSe_2$,[17] PbS,[18] and PbSe,[19] have been demonstrated with great potency for optical and optoelectronic utilizations in the infrared (IR) regime. For example, tin selenide (SnSe) is an important p-type semiconductor with indirect and direct band gaps of 0.90−1.12 and 1.30−1.55 eV, respectively, which are similar to those of typical solar cell materials (*e.g.*, Si and CdTe), capable of absorbing most of the solar spectrum as ideal photovoltaic materials.[20−22] Apart from solar cells, SnSe has also attracted much attention in the application fields of storage switching devices[23] and photodetectors.[15,16] In this regard, various SnSe nanostructures,[15,16,20,23−25] especially in the geometry of NWs,[21,26−28] have been extensively

Received: May 2, 2018
Accepted: June 21, 2018
Published: June 21, 2018

Downloaded via CITY UNIV OF HONG KONG on August 8, 2018 at 06:39:25 (UTC).
See https://pubs.acs.org/sharingguidelines for options on how to legitimately share published articles.

ACS Publications © 2018 American Chemical Society

DOI: 10.1021/acsnano.8b03291
ACS Nano 2018, 12, 7239−7245

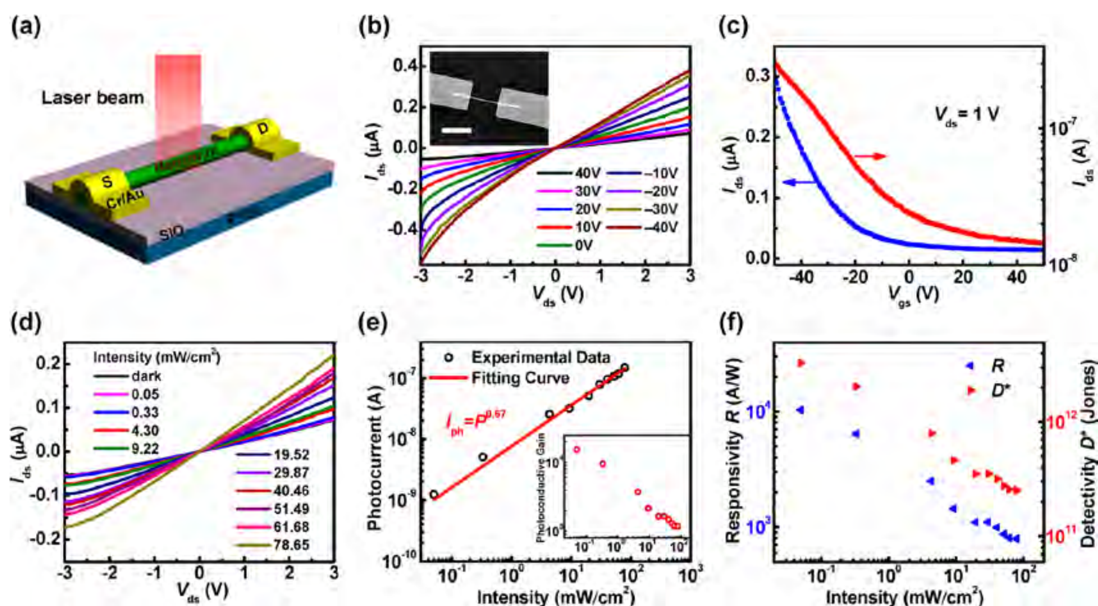

Figure 1. Electrical and optoelectronic properties of a typical SnSe NW FET. (a) Schematic diagram of the single SnSe NW FET photodetector. (b) I_{ds}−V_{ds} output characteristics at various gate voltages from −40 to 40 V. The inset is the SEM image of the SnSe NW FET, scale bar: 3 μm. (c) Linear and logarithmic plot of I_{ds}−V_{gs} transfer characteristics at V_{ds} = 1 V. (d) I_{ds}−V_{ds} output characteristics of the SnSe NW photodetector in the dark and under illumination of a 830 nm laser, measured without additional gate voltage. (e) Measured photocurrent and calculated photoconductive gain (the inset) for different incident light intensities, V_{ds} = 3 V. (f) Calculated photoresponsivity and detectivity at different light power intensities.

investigated. Particularly, Shen *et al.* developed a rapid synthesis technique for SnSe NWs using an ethylenediamine-assisted polyol but accompanyied with a low yield.[26] Likewise, Zhao and his team achieved the synthesis of polycrystalline SnSe NWs with high yields by utilizing a template-assisted approach,[27] while Liu *et al.* could significantly enhance the crystallinity of SnSe NWs with a diameter down to 20 nm *via* a combination of solution-phase synthesis and a seed-inducing method. It is noted that the prepared SnSe NWs could be reliably controlled in length with significant quantum confinement effects; however, the employed synthetic method was rather complex, and toxic reagents were used in the NW growth.[21] In view of all these challenges, without using any complicated process, Butt and his group successfully accomplished the fabrication of high-quality SnSe NWs by conventional chemical vapor deposition (CVD).[28]

At the same time, tin sulfide (SnS) is another essential p-type IV−VI semiconductor with indirect and direct band gaps of 1.2−1.5 and 1.0−1.2 eV, correspondingly. Similar to SnSe NWs, SnS NWs have also been shown with promising prospects as active components in field emitters,[29] battery materials,[10] gas sensors,[11] photodetectors,[30−32] and solar cells.[22] Until now, although a majority of the work has been focused on the synthesis of SnSe and SnS NWs,[29,33−35] very limited study on their electrical and optoelectronic properties for device applications (*e.g.*, highly efficient photodetectors) has been reported. Surprisingly, it is as well found that most of the NW-based photodetector studies are primarily based on the n-type channel material. As a result, it becomes fundamentally important to explore optoelectronic properties of p-type SnSe and SnS NWs in a more systematic manner for high-performance photodetection.

In this work, we synthesize both p-type SnSe and SnS NWs by utilizing a simple CVD method and effectively achieve single SnSe and SnS NW based photodetectors with impressive performances. The electrical and optoelectronic properties of these NW devices are characterized at room temperature in detail. Specifically, the single SnSe and SnS NW photodetectors are found to exhibit a high photoconductive gain, considerable specific detectivity, and fast response time under near-infrared illumination. All these results evidently indicate that the p-type SnSe and SnS NWs would have a wide potential for applications in high-performance photodetectors as well as other advanced optoelectronic devices.

RESULTS AND DISCUSSION

SnSe NWs with excellent crystallinity were synthesized *via* the CVD method in a tube furnace (see the Methods section and Figure S1 in the Supporting Information). To explore the electrical and optoelectronic properties of SnSe NWs, single SnSe NWs were transferred onto Si/SiO_2 substrates and fabricated into field-effect transistors (FETs) using electron-beam lithography (EBL), thermal evaporation of metals, and standard lift-off processes. A schematic illustration of the NW device is given in Figure 1a, while the scanning electron microscope (SEM) image of a typical SnSe NW FET is shown in Figure 1b inset. Specifically, it is observed that the SnSe NW diameter (d) is approximately 80 nm, and the channel length (L) is 3.0 μm. The output and transfer characteristics of the NW devices, as shown in Figure 1b and c, were measured at various gate voltages with an interval of 10 V at room temperature. The linear relationship of I_{ds}−V_{ds} indicates that the contacts between the SnSe NW and metal electrodes are ohmic-like. When V_{gs} decreases from +40 V to −40 V, I_{ds} gradually increases, exhibiting the typical p-type semiconducting behavior. The corresponding I_{ds}−V_{gs} characteristics at V_{ds} = 1 V (Figure 1c) also illustrate the same decreasing I_{ds} trend as V_{gs} increases, which further confirm the p-type conducting characteristics of SnSe NWs. To estimate the hole mobility (μ_{FE}) of the SnSe NW FET, the formula $\mu_{FE} = g_m L^2/(C_g V_{ds})$[36]

DOI: 10.1021/acsnano.8b03291
ACS Nano 2018, 12, 7239−7245

can be applied, where g_m is the transconductance of the NW FET and C_g is the capacitance and can be determined by the analytical equation $2\pi\varepsilon_0\varepsilon_r L/[\ln(4h/d)]$ as a result of the cylinder on-plane model.[36] Here, ε_0 is the permittivity of free space, ε_r is the relative permittivity of SiO_2, $L = 3.0\ \mu m$ is the channel length, $h = 110$ nm is the thickness of the insulating layer, and $d = 80$ nm is the diameter of the SnSe NW. In this case, the hole mobility is calculated to be 5.6 $cm^2\ V^{-1}\ s^{-1}$.

Importantly, the optoelectronic properties of the fabricated SnSe NW FETs were also specifically investigated at room temperature. As shown in Figure 1d, the typical output characteristics of SnSe NW photodetectors were conducted as a two-terminal device without additional gate voltage, in the dark and under laser illumination ($\lambda = 830$ nm) with different incident light intensities. It is clear that the illuminated current (I_{light}) increases gradually with the increasing light intensity under constant V_{ds}. For instance, at $V_{ds} = 3$ V, the I_{light} of the device under a light intensity of 78.65 mW cm^{-2} is approximately 4 times larger than that in dark conditions (I_{dark}), while the net photocurrent (I_{ph}) under the light intensity of 78.65 mW cm^{-2} is 100 times larger than that under the one of 0.05 mW cm^{-2}. The net photocurrent calculated by $I_{ph} = |I_{light}| - |I_{dark}|$ can also be compiled at the different incident light power intensities. The dependence of I_{ph} on the incident light intensity (P) at $V_{ds} = 3$ V, as shown in Figure 1e, can be accurately fitted by the power law relationship[3,37] of $I_{ph} = cP^k$. Note that the power exponent k is an empirical value and no more than 1 in most cases. Here, we obtain $k = 0.67$ through nonlinear fitting. This result exhibits the nonlinear power-dependence of net photocurrent on power density, indicating the complex processes occurred in the NW channel including electron−hole generation, trapping, and recombination.[3,37]

Based on the photocurrent dependence on light intensity, several key performance parameters of photodetectors, such as photoconductive gain (G), responsivity (R), and detectivity (D^*), can be further evaluated for the NW device. The G is typically defined as the number of electron−hole pairs contributing to the net photocurrent when absorbing one photon and can be written as[4,5] $G = (I_{ph}/e)/(PA/h\nu)$, where e is the electronic charge, A is the effective area, and $h\nu$ is the photon energy. Here we use the cross-sectional area ($A = L \times d$, the product of the channel length and NW diameter) to estimate the effective irradiated area of the SnSe NW photodetector.[4,6] The Figure 1e inset also presents the gain of the photodetector at different light intensities. It is shown that the gain is as high as 1.5×10^4 under a light intensity of 0.05 mW cm^{-2} at $V_{ds} = 3$ V, in which this high gain could be interpreted as photogating.[3] On the other hand, the gain of photoconductors can as well be estimated by τ/τ_T, where τ is the minority carrier lifetime and τ_T is the corresponding carrier transit time. Specifically, under a bias of 3 V, considering a channel length of 3 μm and hole mobility of 5.6 $cm^2\ V^{-1}\ s^{-1}$, the carrier transit time can be approximately assessed as $\tau_T = L^2/\mu V_{ds} = 6 \times 10^{-9}$ s. This result would then lead to an estimated carrier lifetime of around $10^2\ \mu s$, which can be further verified by the temporal photoresponse measurement in the following experiments. Moreover, the gain is observed to decrease gradually with the increasing light intensity, which could be attributed to the saturation and recombination of photogenerated electron−hole pairs.[5] High optical gain originated from the prolonged excess carrier lifetime also directly leads to a longer photoresponse time or a slower response speed, thus limiting the bandwidth. It is hard to improve both the gain and bandwidth at the same time. Even for the traditional thin-film avalanched photodiodes (APD), which can achieve high gain, in some cases their gain should be restricted to ensure the bandwidth. For our SnSe devices, the response time is as fast as hundreds of microseconds, while the gain is as high as 10^4. In any case, this relatively high gain of the fabricated photodetector demonstrates clearly that a substantially large photocurrent can be achieved under a weak incident light intensity, revealing the potential of our SnSe NWs for highly sensitive photodetection.[4,37]

Besides, there are another two additional key parameters, responsivity (R) and specific detectivity (D^*), to evaluate the photodetector performance. Responsivity is defined as[4,38,39] $R = I_{ph}/(PA)$, describing the ability of a detector to convert incident light intensities into electrical signals. Specific detectivity of a photodetector is used to characterize the minimum detectable signal. It can be expressed as[4,40] $D^* = (AB)^{1/2}/(\mathrm{NEP})$, where NEP is the noise equivalent power and B is the electrical bandwidth. Since the shot noise is typically considered as the major noise source, the specific detectivity can be simply expressed as[4,6,40] $D^* = RA^{1/2}/(2eI_{dark})^{1/2}$. Here we ignore the Johnson noise (see the comparison between the shot noise and thermal noise in the Supporting Information). In this case, both the calculated R and D^*, as shown in Figure 1f, increase significantly with the decreasing light intensity, in which R and D^* can be enhanced to as much as 1.0×10^4 A W^{-1} and 3.3×10^{12} Jones, respectively, at $V_{ds} = 3$ V and under the low incident light intensity of 0.05 mW cm^{-2}. These optimal R and D^* values of the NW device are readily comparable to those of the commercially available photodetectors based on Si, Ge, or InGaAs.[40−42]

To investigate the capability of our SnSe NW photodetectors to follow a fast varying optical signal, time-resolved photocurrent measurements were conducted by periodically modulating the illumination cycle of the near-infrared laser of 830 nm. Explicitly, Figure 2a depicts the photocurrent trace of

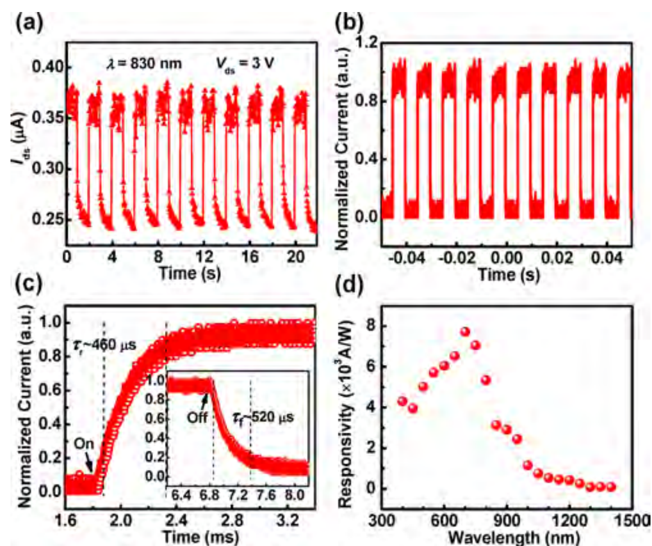

Figure 2. Time response and spectral response characterizations of a typical single SnSe NW photodetector. (a) Photocurrent trace of the device illuminated by a chopped light with a frequency of 0.5 Hz at $V_{ds} = 3$ V and $V_{gs} = 0$ V. (b) Time-resolved photocurrent response of the device at a chopping frequency of 100 Hz. (c) Rise and fall times of the high-resolution photocurrent response of the device. (d) Spectral response of the device at a number of discrete illumination wavelengths from 400 to 1400 nm under a light intensity of 0.92 mW cm^{-2} and at a bias of 1 V.

DOI: 10.1021/acsnano.8b03291
ACS Nano 2018, 12, 7239−7245

the device under a light intensity of 78.65 mW cm^{-2} with a chopping frequency of 1 Hz, at V_{ds} = 3 V and V_{gs} = 0 V. It is clear that the efficient switching behavior indicates the good periodicity and stability of the NW device (also see photocurrent measured at different light intensities in Supporting Information Figure S2a). Furthermore, a digital oscilloscope was connected to the measurement system to monitor and capture the fast-varying photocurrent signals,[37,43] which helped to accurately evaluate the rise and fall time constants of the device. Figure 2b and c show the high-resolution time-dependent photocurrent response of the device at a chopping frequency of 100 Hz (also see time-resolved photoresponse at 1 kHz chopping in Supporting Information Figure S2b). Evidently, a rise time of 460 μs and a fall time of 520 μs were obtained. Here we consider the time it takes for the net photocurrent to increase from 10% to 90% (or decrease from 90% to 10%) as the rise time (or fall time). The relatively fast response speed indicates the fast generation and recombination process of electron−hole pairs occurred in the NWs when under illumination, which could be attributed to the good NW crystal quality and fewer surface states. In addition, the eye diagram measurement can also demonstrate this considerable response speed of the NW photodetector (see Supporting Information Figure S4). It is as well noted that these response speeds may vary due to the dissimilar device channel control of the different applied gate voltage. In particular, at the same V_{ds}, both photocurrent and responsivity of the device at V_{gs} of −40 V are found to be larger than those measured at V_{gs} of +40 V (see Supporting Information Figure S2c,d), in which this behavior is probably contributed by the p-type nature of SnSe NWs such that the electron traps play an important role at the larger negative gate voltages.[3]

On top of the above-discussed performance data, evaluating the spectral response is also critical for the development of advanced NW photodetectors. In this work, the photocurrents at a number of discrete illumination wavelengths from 400 to 1400 nm were measured under a light intensity of 0.92 mW cm^{-2} and at a bias of 1 V, as shown in Figure 2d. It is observed that the responsivity is maximized around the wavelength of 700 nm and then sharply decays for wavelengths longer than 800 nm. It also can be observed that there is still an appreciable photoresponse even at a wavelength of 1200 nm. This maximum detectable wavelength is perfectly consistent with the band gap of SnSe NWs. The photoresponse measurements of SnSe NW photodetectors were also performed at different illumination wavelengths (see Supporting Information Figure S3a−d). All these findings illustrate the excellent spectral response characteristics of SnSe NW devices from visible to near-infrared wavelengths, which can enable the high-performance photodetection over a wide spectrum range.

To further shed light on the photodetection mechanism of SnSe NW devices, scanning photocurrent microscopy was conducted at different bias voltages.[43] In short, the measurements were performed under atmospheric conditions using a laser beam (λ = 637 nm) focused onto the device using a 100× objective len. Figure 3a−c displays the spatially resolved photocurrent mapping of the device at V_{ds} of 0.1, 1, and 3 V, respectively. The outlines of the electrodes are depicted by using the white dotted lines. It is found that photocurrents with opposite polarities are generated at the contact regions between the NW and the metal electrodes at V_{ds} = 0.1 V (see Figure 3a, the dim region implies a negative photocurrent generation, while the bright region denotes positive photocurrent generation). When V_{ds} increases to 1 V, the negative

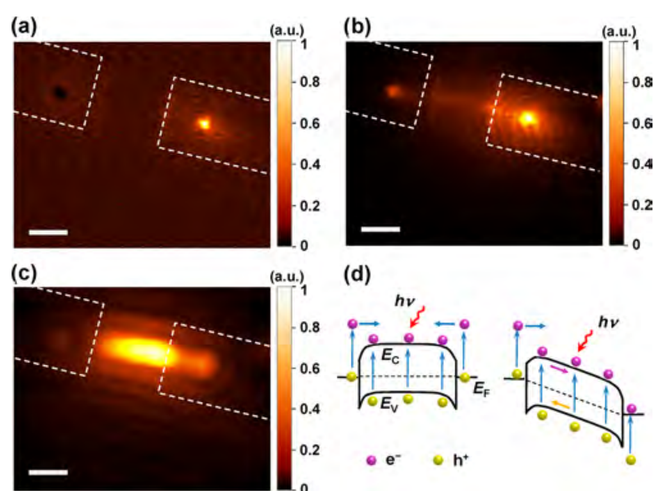

Figure 3. Scanning photocurrent mapping of the single SnSe NW photodetector at bias voltages of (a) 0.1 V, (b) 1 V, and (c) 3 V. The laser with a wavelength of 637 nm and power of 200 μW was used. White dotted lines are used to show the outlines of the electrodes, scale bar: 2 μm. (d) Energy band diagrams of the device under illumination at the equilibrium (left) state and under a source−drain bias (right).

photocurrent signals disappear, and the weak positive photocurrent signals are then observed at the NW channel (Figure 3b). For a larger V_{ds} bias of 3 V, the strong photocurrents are generated and witnessed throughout the entire NW channel (Figure 3c). It is clear that the photocurrent signals are strongly dependent on the source−drain bias, which can be interpreted by the corresponding band diagrams shown in Figure 3d. When the drain is applied with a small bias voltage as low as 0.1 V, the contact barrier between the NW and the source electrode is not fully overcome, while a majority of voltage drop occurs at the region of source contact. In this case, the Schottky junctions established at the metal/NW interfaces would dominate the voltage; an insignificant voltage drop takes place across the NW channel in equilibrium as shown in Figure 3a. As a result, the generation and separation of electron−hole pairs in the Schottky junction region would contribute dominantly to the photocurrent, leading to the mapping signals with opposite polarities.[7,44−46] When V_{ds} increases to 1 V, the contact barrier is overcome and the bias voltage drop mainly occurs across the NW channel (see Figure 3b), which leads to the vanishing of the negative photocurrent signal. At the same time, the weak positive photocurrent is generated from the NW channel because of the increased carrier drift distance driven by the larger external electric field. At V_{ds} = 3 V, more photon-generated carriers are collected by the source and drain electrodes under the larger bias voltage, resulting in a stronger photocurrent signal across the entire NW channel, as presented in Figure 3c. All these findings have furthered the insight into the photodetection mechanism of the SnSe NW devices.

Additionally, SnS NWs and their photodetectors were also successfully prepared and characterized (see Supporting Information Figure S5). Specifically, the detailed electrical and optoelectronic measurements of single SnS NW FETs were systematically performed. Figure 4a depicts the transfer characteristics of a typical single SnS NW FET at a bias of 1 V, while the inset gives the corresponding SEM image of the device with d = 90 nm and L = 3.2 μm. The transfer curves clearly indicate that the device is a p-type FET with the calculated μ_{FE} of 0.5 cm^2 V^{-1} s^{-1}. Interestingly, the contacts

DOI: 10.1021/acsnano.8b03291
ACS Nano 2018, 12, 7239−7245

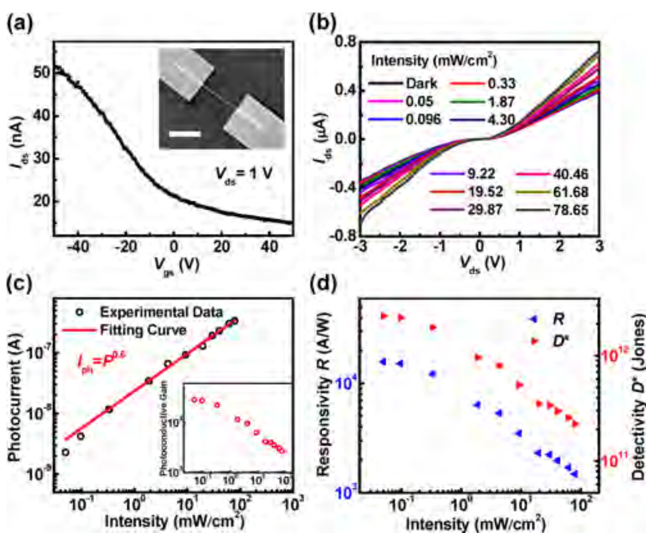

Figure 4. Electrical and optoelectronic properties of the single SnS NW FET. (a) I_{ds}−V_{gs} transfer characteristics at V_{ds} = 1 V. The inset is the SEM image, scale bar: 2 μm. (b) Output characteristics in dark and under illumination of a 830 nm laser, without additional gate voltage. (c) Dependence of photocurrent and optical gain (the inset) on the incident light power intensity, V_{ds} = 3 V. (d) Responsivity and detectivity of the SnS NW photodetector at various light power intensities.

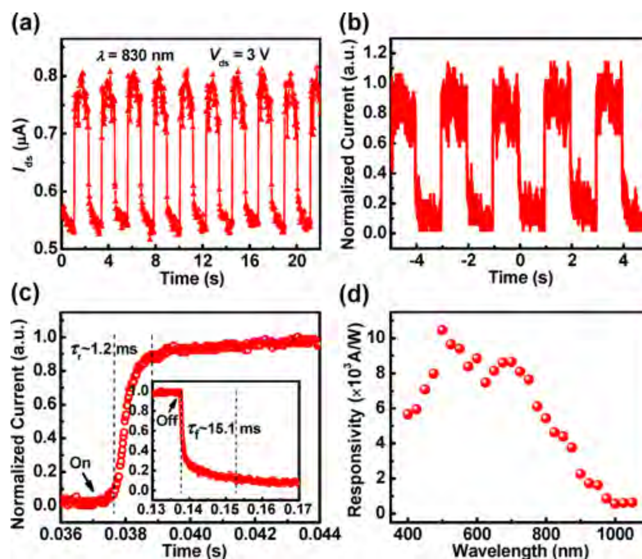

Figure 5. Characterizations on the time response and spectral response of the single SnS NW photodetector. (a) Photocurrent response of the device under optical chopping of 0.5 Hz at V_{ds} = 3 V and V_{gs} = 0 V. (b) Time-resolved photocurrent response of the device at a chopping frequency of 1 Hz. (c) Rise and fall times of the device extracted from the high-resolution photocurrent response. (d) Spectral response of the device at a number of discrete wavelengths from 400 to 1050 nm at the same light intensity of 2 mW cm^{-2}.

between the NW and metal electrodes are Schottky instead of ohmic-like (see I_{ds}−V_{ds} curves of the SnS NW FET at different gate voltages in Supporting Information Figure S6a,b), suggesting a high potential barrier exists between the SnS NW and metal electrodes. In order to investigate the dependence of detector photoresponse on the incident light intensity, the I_{ds}−V_{ds} curves were measured under an illumination of 830 nm for different light intensities, without additional gate voltage as shown in Figure 4b. Then, the I_{ph} could be extracted with different light intensities at V_{ds} = 3 V and compiled with a fitted power law equation of I_{ph} = $P^{0.6}$, as given in Figure 4c. Also, the Figure 4c inset displays the calculated optical gain of the SnS NW photodetector (V_{ds} = 3 V). The gain is found to be up to 2.8 × 10^4 for the light intensity of 0.05 mW cm^{-2}. Responsivity and detectivity of the photodetector can as well be obtained at different power intensities as presented in Figure 4d. It is obvious that both R and D* can be as high as 1.6 × 10^4 A W^{-1} and 2.4 × 10^{12} Jones, respectively, in which these two performance parameters are certainly comparable to those of SnSe NW devices.

Importantly, the photoresponse of a typical SnS NW photodetector was also thoroughly evaluated under 830 nm illumination with a chopping frequency of 1 Hz at V_{ds} = 3 V and V_{gs} = 0 V, as shown in Figure 5a. The high-resolution time response illustrates that the rise time and fall time of the SnS NW detector are approximately 1.2 and 15.1 ms, respectively (see Figure 5b,c). Even though the response speed is relatively fast, being on the order of one millisecond, this speed is still slower than that of the SnSe NW photodetector. Besides, it is found that the fall time is much longer than the rise time in SnS NW photodetectors, which is different from that in our SnSe devices and other conventional detectors, wherein the rise time and fall time are almost on the same order of magnitude. Surface states or trap centers could respond to this phenomenon. Because of them, the trapped carriers are hard to be released. As a result, the recombination process of excess carriers are slowed down, leading to a longer fall time. In some extreme cases, trap states can even lead to persistent positive or negative photocurrent.[37,46,47]

In the meanwhile, the time response of the SnS NW photodetector was also assessed under different light intensities at 830 nm illumination as well as at other various wavelengths (see Supporting Information Figure S7 and Figure S8a−d). Notably, the device has no significant response to the near-infrared illumination with incident light of wavelengths longer than 1060 nm. Moreover, similar results are obtained from the scanning photocurrent mapping performed on the SnS NW photodetector, which suggests that both SnSe and SnS NW devices share the same photoresponse mechanism (see Supporting Information Figure S9). The photoresponse spectra of the single SnS NW device are then evaluated in detail at a number of discrete wavelengths from 400 to 1050 nm with the same light intensity of 2 mW cm^{-2}, as presented in Figure 5d. It is observed that the responsivity is maximized at λ = 500 nm. When the wavelength is longer than 750 nm, the responsivity decreases sharply with the increasing incident light wavelength. In any case, there is still an appreciable photoresponse at the wavelength of 1000 nm, which demonstrates the broadband photodetection capability of our NWs spanning a waveband from visible to near-infrared.

CONCLUSIONS

In summary, both p-type SnSe and SnS NWs are successfully synthesized by the CVD method, followed by the fabrication of their single NW photodetectors. These NW devices exhibit a high photoconductive gain, good responsivity, excellent detectivity, and fast response speed under near-infrared illumination. In addition, these devices also show broadband photoresponse over visible to near-infrared wavelengths. Based on the spatially resolved scanning photocurrent mapping, the photocurrent is typically observed at the metal−semiconductor Schottky

DOI: 10.1021/acsnano.8b03291
ACS Nano 2018, 12, 7239−7245

junction as well as across the NW channel, which is highly dependent on the applied voltage bias. All these results evidently demonstrate that these p-type SnSe and SnS NWs have enormous potentials for next-generation highly sensitive, fast-response, and broadband optoelectronic devices.

METHODS

Nanowire Synthesis. The SnSe and SnS NWs were synthesized on the Si substrate *via* a CVD method. In detail, the source material, SnSe (or SnS) powder (0.1 g; 99.999% purity), was first placed at the center of a quartz tube, while a Si substrate coated with a Au film (∼1 nm thick) was placed at the downstream side about 12−15 cm away from the powder source. For the growth of SnSe NWs, the tube was first evacuated to a pressure of lower than 1×10^{-3} mbar; then a mixture of carrier gas of Ar and H_2 (20%) was introduced into the tube at a constant flow rate of 100 sccm (standard-state cubic centimeter per minute). Subsequently, the SnSe powder was heated to 750 °C, while maintaining the pressure at 300 mbar. After 30 min of duration, the heating was stopped and the system was cooled naturally. For the growth of SnS NWs, the furnace temperature is 700 °C instead of 750 °C. Finally, the system was naturally cooled to room temperature. Consequently, numerous vertically standing NWs can be found on the growth substrate.

Fabrication and Characterization of Photodetectors. The NWs were first transferred onto the Si/SiO_2 (110 nm thick thermally grown oxide) substrate with patterned marks. Electron-beam lithography (JEOL 6510 SEM with NPGS controlling system) was employed to define the drain and source electrodes, and thermal evaporation was subsequently used to deposit the Cr/Au (15 nm/50 nm) electrodes. Before depositing the metal, the NWs were immersed into a diluted 2% HF solution for 10 s to remove the native oxide layer on the NW surface. The electrical and optoelectronic measurements of the NW FETs were conducted by a Keithley 4200 semiconductor parameter analyzer combined with a Lake Shore TTPX probe station at room temperature. The time-resolved photocurrent measurements of the device were performed by laser irradiations with square wave modulation and recorded by a digital oscilloscope at a sampling frequency of 1 MHz. For photocurrent mapping, the scanning Galvo System (Thorlabs GVS212) was used to scan the chopped laser in a two-dimensional plane, and a Signal Recovery model 7270 lock-in amplifier was used to lock the spatially resolved photocurrent mapping signals. Then both the $x-y$ positions of the laser spot and photocurrents of the device were processed by the GXSM software through a scanning probe microscope controlling system to achieve real-time imaging.

ASSOCIATED CONTENT

Supporting Information

The Supporting Information is available free of charge on the ACS Publications website at DOI: 10.1021/acsnano.8b03291.

Experimental procedure including nanowire synthesis, sample characterizations, and additional photoelectronic measurements as well as figures (Figures S1−S9) (PDF)

AUTHOR INFORMATION

Corresponding Authors

*E-mail: longms@mail.sitp.ac.cn.
*E-mail: liaolei@whu.edu.cn.
*E-mail: wdhu@mail.sitp.ac.cn.

ORCID

Hehai Fang: 0000-0001-8393-9264
Xing Wu: 0000-0002-9207-6744
Johnny C. Ho: 0000-0003-3000-8794
Lei Liao: 0000-0003-1325-2410
Weida Hu: 0000-0001-5278-8969

Author Contributions

¶D. Zheng and H. Fang contributed equally to this work.

Author Contributions

W.H., M.L., and L.L. conceived and supervised the research. D.Z. grew the nanowires. H.F. and D.Z. fabricated the NW FETs and performed most of the measurements. X.W. conducted the HR-TEM. D.Z, H.F., and W.H. wrote the paper. All authors discussed the results and revised the manuscript.

Notes

The authors declare no competing financial interest.

ACKNOWLEDGMENTS

This work was supported by the National Natural Science Foundation of China (Grant Nos. 61725505, 11734016, and 61521005), Key Research Project of Frontier Science of Chinese Academy of Sciences (Grant No. QYZDB-SSW-JSC031), Fund of Shanghai Natural Science Foundation (Grant No. 18ZR1445800), Hubei Province Natural Science Foundation (Grant No. 2018CFB567), Royal Society-Newton Advanced Fellowship (Grant No. NA170214), CAS Interdisciplinary Innovation Team, and National Program for Support of Top-notch Young Professionals. In addition, the authors would like to specially thank James Torley from the University of Colorado for his valuable comments on the manuscript.

REFERENCES

(1) Wang, J.; Gudiksen, M. S.; Duan, X.; Cui, Y.; Lieber, C. M. Highly Polarized Photoluminescence and Photodetection from Single Indium Phosphide Nanowires. *Science* **2001**, *293*, 1455−1457.
(2) Duan, X. F.; Huang, Y.; Cui, Y.; Wang, J. F.; Lieber, C. M. Indium Phosphide Nanowires as Building Blocks for Nanoscale Electronic and Optoelectronic Devices. *Nature* **2001**, *409*, 66−69.
(3) Fang, H.; Hu, W. Photogating in Low Dimensional Photodetectors. *Adv. Sci.* **2017**, *4*, 1700723.
(4) Liu, X.; Gu, L.; Zhang, Q.; Wu, J.; Long, Y.; Fan, Z. All-Printable Band-Edge Modulated ZnO Nanowire Photodetectors with Ultra-High Detectivity. *Nat. Commun.* **2014**, *5*, 4007.
(5) Soci, C.; Zhang, A.; Xiang, B.; Dayeh, S. A.; Aplin, D. P. R.; Park, J.; Bao, X. Y.; Lo, Y. H.; Wang, D. ZnO Nanowire UV Photodetectors with High Internal Gain. *Nano Lett.* **2007**, *7*, 1003−1009.
(6) Zheng, D.; Wang, J.; Hu, W.; Liao, L.; Fang, H.; Guo, N.; Wang, P.; Gong, F.; Wang, X.; Fan, Z.; Wu, X.; Meng, X.; Chen, X.; Lu, W. When Nanowires Meet Ultrahigh Ferroelectric Field-High-Performance Full-Depleted Nanowire Photodetectors. *Nano Lett.* **2016**, *16*, 2548−2555.
(7) Zheng, D.; Fang, H.; Wang, P.; Luo, W.; Gong, F.; Ho, J. C.; Chen, X.; Lu, W.; Liao, L.; Wang, J.; Hu, W. High-Performance Ferroelectric Polymer Side-Gated CdS Nanowire Ultraviolet Photodetectors. *Adv. Funct. Mater.* **2016**, *26*, 7690−7696.
(8) Wallentin, J.; Anttu, N.; Asoli, D.; Huffman, M.; Aberg, I.; Magnusson, M. H.; Siefer, G.; Fuss-Kailuweit, P.; Dimroth, F.; Witzigmann, B.; Xu, H. Q.; Samuelson, L.; Deppert, K.; Borgstrom, M. T. InP Nanowire Array Solar Cells Achieving 13.8% Efficiency by Exceeding the Ray Optics Limit. *Science* **2013**, *339*, 1057−1060.
(9) Mahdi, M. S.; Ibrahim, K.; Hmood, A.; Ahmed, N. M.; Azzez, S. A.; Mustafa, F. I. A Highly Sensitive Flexible SnS Thin Film Photodetector in the Ultraviolet to Near Infrared Prepared by Chemical Bath Deposition. *RSC Adv.* **2016**, *6*, 114980−114988.
(10) Lu, J.; Nan, C.; Li, L.; Peng, Q.; Li, Y. Flexible SnS Nanobelts: Facile Synthesis, Formation Mechanism and Application in Li-ion Batteries. *Nano Res.* **2013**, *6*, 55−64.
(11) Lu, F.; Yang, J.; Li, R.; Huo, N.; Li, Y.; Wei, Z.; Li, J. Gas-Dependent Photoresponse of SnS Nanoparticles-Based Photodetectors. *J. Mater. Chem. C* **2015**, *3*, 1397−1402.
(12) Gong, Y.; Yuan, H.; Wu, C.-L.; Tang, P.; Yang, S.-Z.; Yang, A.; Li, G.; Liu, B.; van de Groep, J.; Brongersma, M. L.; Chisholm, M. F.;

DOI: 10.1021/acsnano.8b03291
ACS Nano 2018, 12, 7239−7245

Zhang, S.-C.; Zhou, W.; Cui, Y. Spatially Controlled Doping of Two-Dimensional SnS_2 Through Intercalation for Electronics. *Nat. Nanotechnol.* **2018**, *13*, 294−299.

(13) Su, G.; Hadjiev, V. G.; Loya, P. E.; Zhang, J.; Lei, S.; Maharjan, S.; Dong, P.; P, M. A.; Lou, J.; Peng, H. Chemical Vapor Deposition of Thin Crystals of Layered Semiconductor SnS_2 for Fast Photodetection Application. *Nano Lett.* **2015**, *15*, 506−513.

(14) Liu, X.; Li, Y.; Zhou, B.; Wang, X.; Cartwright, A. N.; Swihart, M. T. Shape-Controlled Synthesis of SnE (E = S, Se) Semiconductor Nanocrystals for Optoelectronics. *Chem. Mater.* **2014**, *26*, 3515−3521.

(15) Li, L.; Chen, Z.; Hu, Y.; Wang, X.; Zhang, T.; Chen, W.; Wang, Q. Single-Layer Single-Crystalline SnSe Nanosheets. *J. Am. Chem. Soc.* **2013**, *135*, 1213−1216.

(16) Cao, J.; Wang, Z.; Zhan, X.; Wang, Q.; Safdar, M.; Wang, Y.; He, J. Vertical SnSe Nanorod Arrays: From Controlled Synthesis and Growth Mechanism to Thermistor and Photoresistor. *Nanotechnology* **2014**, *25*, 105705.

(17) Huang, Y.; Xu, K.; Wang, Z.; Shifa, T. A.; Wang, Q.; Wang, F.; Jiang, C.; He, J. Designing the Shape Evolution of $SnSe_2$ Nanosheets and Their Optoelectronic Properties. *Nanoscale* **2015**, *7*, 17375−17380.

(18) Wen, Y.; Wang, Q.; Yin, L.; Liu, Q.; Wang, F.; Wang, F.; Wang, Z.; Liu, K.; Xu, K.; Huang, Y.; Shifa, T. A.; Jiang, C.; Xiong, J.; He, J. Epitaxial 2D PbS Nanoplates Arrays with Highly Efficient Infrared Response. *Adv. Mater.* **2016**, *28*, 8051−8057.

(19) Graham, R.; Yu, D. High Carrier Mobility in Single Ultrathin Colloidal Lead Selenide Nanowire Field Effect Transistors. *Nano Lett.* **2012**, *12*, 4360−4365.

(20) Franzman, M. A.; Schlenker, C. W.; Thompson, M. E.; Brutchey, R. L. Solution-Phase Synthesis of SnSe Nanocrystals for Use in Solar Cells. *J. Am. Chem. Soc.* **2010**, *132*, 4060−4061.

(21) Liu, S.; Guo, X.; Li, M.; Zhang, W. H.; Liu, X.; Li, C. Solution-Phase Synthesis and Characterization of Single-Crystalline SnSe Nanowires. *Angew. Chem., Int. Ed.* **2011**, *50*, 12050−12053.

(22) Pejjai, B.; Minnam Reddy, V. R.; Gedi, S.; Park, C. Status Review on Earth-Abundant and Environmentally Green SnX (X = Se, S) Nanoparticle Synthesis by Solution Methods for Photovoltaic Applications. *Int. J. Hydrogen Energy* **2017**, *42*, 2790−2831.

(23) Chun, D.; Walser, R. M.; Bené, R. W.; Courtney, T. H. Polarity-Dependent Memory Switching in Devices with SnSe and $SnSe_2$ Crystals. *Appl. Phys. Lett.* **1974**, *24*, 479−481.

(24) Xia, J.; Zhu, D.; Li, X.; Wang, L.; Tian, L.; Li, J.; Wang, J.; Huang, X.; Meng, X.-M. Epitaxy of Layered Orthorhombic SnS-SnS_xSe_{1-x} Core-Shell Heterostructures with Anisotropic Photoresponse. *Adv. Funct. Mater.* **2016**, *26*, 4673−4679.

(25) Han, G.; Popuri, S. R.; Greer, H. F.; Bos, J. W.; Zhou, W.; Knox, A. R.; Montecucco, A.; Siviter, J.; Man, E. A.; Macauley, M.; Paul, D. J.; Li, W. G.; Paul, M. C.; Gao, M.; Sweet, T.; Freer, R.; Azough, F.; Baig, H.; Sellami, N.; Mallick, T. K.; et al. Facile Surfactant-Free Synthesis of *p*-type SnSe Nanoplates with Exceptional Thermoelectric Power Factors. *Angew. Chem., Int. Ed.* **2016**, *55*, 6433−6437.

(26) Shen, G.; Chen, D.; Jiang, X.; Tang, K.; Liu, Y.; Qian, Y. Rapid Synthesis of SnSe Nanowires *via* an Ethylenediamine-Assisted Polyol Route. *Chem. Lett.* **2003**, *32*, 426−427.

(27) Zhao, L.; Yosef, M.; Steinhart, M.; Goring, P.; Hofmeister, H.; Gosele, U.; Schlecht, S. Porous Silicon and Alumina as Chemically Reactive Templates for the Synthesis of Tubes and Wires of SnSe, Sn, and SnO_2. *Angew. Chem., Int. Ed.* **2005**, *45*, 311−315.

(28) Butt, F. K.; Mirza, M.; Cao, C.; Idrees, F.; Tahir, M.; Safdar, M.; Ali, Z.; Tanveer, M.; Aslam, I. Synthesis of Mid-Infrared SnSe Nanowires and Their Optoelectronic Properties. *CrystEngComm* **2014**, *16*, 3470.

(29) Suryawanshi, S. R.; Warule, S. S.; Patil, S. S.; Patil, K. R.; More, M. A. Vapor-Liquid-Solid Growth of One-Dimensional Tin Sulfide (SnS) Nanostructures with Promising Field Emission Behavior. *ACS Appl. Mater. Interfaces* **2014**, *6*, 2018−2025.

(30) Zhou, X.; Gan, L.; Zhang, Q.; Xiong, X.; Li, H.; Zhong, Z.; Han, J.; Zhai, T. High Performance Near-Infrared Photodetectors Based on Ultrathin SnS nanobelts Grown *via* Physical Vapor Deposition. *J. Mater. Chem. C* **2016**, *4*, 2111−2116.

(31) Deng, Z.; Cao, D.; He, J.; Lin, S.; Lindsay, S. M.; Liu, Y. Solution Synthesis of Ultrathin Single-Crystalline SnS Nanoribbons for Photodetectors *via* Phase Transition and Surface Processing. *ACS Nano* **2012**, *6*, 6197−6207.

(32) Chao, J.; Wang, Z.; Xu, X.; Xiang, Q.; Song, W.; Chen, G.; Hu, J.; Chen, D. Tin Sulfide Nanoribbons as High Performance Photoelectrochemical Cells, Flexible Photodetectors and Visible-Light-Driven Photocatalysts. *RSC Adv.* **2013**, *3*, 2746.

(33) Yue, G.; Lin, Y.; Wen, X.; Wang, L.; Peng, D. SnS Homojunction Nanowire-Based Solar Cells. *J. Mater. Chem.* **2012**, *22*, 16437.

(34) Yue, G. H.; Lin, Y. D.; Wen, X.; Wang, L. S.; Chen, Y. Z.; Peng, D. L. Synthesis and Characterization of The SnS Nanowires *via* Chemical Vapor Deposition. *Appl. Phys. A: Mater. Sci. Process.* **2012**, *106*, 87−91.

(35) Panda, S. K.; Datta, A.; Dev, A.; Gorai, S.; Chaudhuri, S. Surfactant-Assisted Synthesis of SnS Nanowires Grown on Tin Foils. *Cryst. Growth Des.* **2006**, *6*, 2177−2181.

(36) Zou, X.; Liu, X.; Wang, C.; Jiang, Y.; Wang, Y.; Xiao, X.; Ho, J. C.; Li, J.; Jiang, C.; Xiong, Q.; Liao, L. Controllable Electrical Properties of Metal-Doped In_2O_3 Nanowires for High-Performance Enhancement Mode Transistors. *ACS Nano* **2013**, *7*, 804−810.

(37) Guo, N.; Hu, W.; Liao, L.; Yip, S.; Ho, J. C.; Miao, J.; Zhang, Z.; Zou, J.; Jiang, T.; Wu, S.; Chen, X.; Lu, W. Anomalous and Highly Efficient InAs Nanowire Phototransistors Based on Majority Carrier Transport at Room Temperature. *Adv. Mater.* **2014**, *26*, 8203−8209.

(38) Miao, J. S.; Hu, W. D.; Guo, N.; Lu, Z. Y.; Zou, X. M.; Liao, L.; Shi, S. X.; Chen, P. P.; Fan, Z. Y.; Ho, J. C.; Li, T. X.; Chen, X. S.; Lu, W. Single InAs Nanowire Room-Temperature Near-Infrared Photodetectors. *ACS Nano* **2014**, *8*, 3628−3635.

(39) Wang, X.; Wang, P.; Wang, J.; Hu, W.; Zhou, X.; Guo, N.; Huang, H.; Sun, S.; Shen, H.; Lin, T.; Tang, M.; Liao, L.; Jiang, A.; Sun, J.; Meng, X.; Chen, X.; Lu, W.; Chu, J. Ultrasensitive and Broadband MoS_2 Photodetector Driven by Ferroelectrics. *Adv. Mater.* **2015**, *27*, 6575−6581.

(40) Gong, X.; Tong, M. H.; Xia, Y. J.; Cai, W. Z.; Moon, J. S.; Cao, Y.; Yu, G.; Shieh, C. L.; Nilsson, B.; Heeger, A. J. High-Detectivity Polymer Photodetectors with Spectral Response from 300 to 1450 nm. *Science* **2009**, *325*, 1665−1667.

(41) Manders, J. R.; Lai, T.-H.; An, Y.; Xu, W.; Lee, J.; Kim, D. Y.; Bosman, G.; So, F. Low-Noise Multispectral Photodetectors Made from All Solution-Processed Inorganic Semiconductors. *Adv. Funct. Mater.* **2014**, *24*, 7205−7210.

(42) For instance, a common GaAs biased photodetector (400−900 nm) has a responsivity of 0.45 A W^{-1} at 850 nm. http://search.newport.com/?q=*&x2=sku&q2=818-BB-45.

(43) Wang, P.; Liu, S.; Luo, W.; Fang, H.; Gong, F.; Guo, N.; Chen, Z. G.; Zou, J.; Huang, Y.; Zhou, X.; Wang, J.; Chen, X.; Lu, W.; Xiu, F.; Hu, W. Arrayed Van Der Waals Broadband Detectors for Dual-Band Detection. *Adv. Mater.* **2017**, *29*, 1604439.

(44) Allen, J. E.; Hemesath, E. R.; Lauhon, L. J. Scanning Photocurrent Microscopy Analysis of Si Nanowire Field-Effect Transistors Fabricated by Surface Etching of the Channel. *Nano Lett.* **2009**, *9*, 1903−1908.

(45) Yoon, K.; Hyun, J. K.; Connell, J. G.; Amit, I.; Rosenwaks, Y.; Lauhon, L. J. Barrier Height Measurement of Metal Contacts to Si Nanowires Using Internal Photoemission of Hot Carriers. *Nano Lett.* **2013**, *13*, 6183−6188.

(46) Fang, H.; Hu, W.; Wang, P.; Guo, N.; Luo, W.; Zheng, D.; Gong, F.; Luo, M.; Tian, H.; Zhang, X.; Luo, C.; Wu, X.; Chen, P.; Liao, L.; Pan, A.; Chen, X.; Lu, W. Visible Light-Assisted High-Performance Mid-Infrared Photodetectors Based on Single InAs Nanowire. *Nano Lett.* **2016**, *16*, 6416−6424.

(47) Jeon, S.; Ahn, S. E.; Song, I.; Kim, C. J.; Chung, U. I.; Lee, E.; Yoo, I.; Nathan, A.; Lee, S.; Robertson, J.; Kim, K. Gated Three-Terminal Device Architecture to Eliminate Persistent Photoconduc-

DOI: 10.1021/acsnano.8b03291
ACS Nano 2018, 12, 7239−7245